Journal of Power Sources 412 (2019) 1–9

Contents lists available at ScienceDirect

Journal of Power Sources

journal homepage: www.elsevier.com/locate/jpowsour

Biomass-derived robust three-dimensional porous carbon for high volumetric performance supercapacitors

Xiaoguang Liu[a], Changde Ma[b], Jiaxin Li[b], Beata Zielinska[a], Ryszard J. Kalenczuk[a], Xuecheng Chen[a,b,*], Paul K. Chu[c,**], Tao Tang[b,***], Ewa Mijowska[a]

[a] Nanomaterials Physicochemistry Department, West Pomeranian University of Technology Szczecin, al. Piastów 45, 70-311, Szczecin, Poland
[b] State Key Laboratory of Polymer Physics and Chemistry, Changchun Institute of Applied Chemistry, Chinese Academy of Sciences, Changchun, 130022, China
[c] Department of Physics and Department of Materials Science and Engineering, City University of Hong Kong, Tat Chee Avenue, Kowloon, Hong Kong, China

HIGHLIGHTS

- Robust three-dimensional porous carbon is prepared.
- The porous carbon has a high particle density.
- The electrochemical test exhibits outstanding volumetric performance.
- Excellent rate capability and superior cycle stability are obtained.

GRAPHICAL ABSTRACT

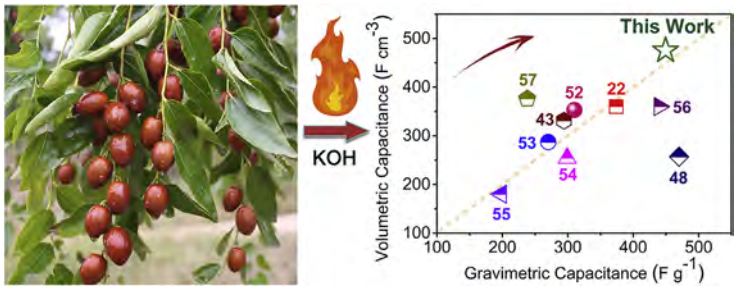

ARTICLE INFO

Keywords:
Robust 3D porous carbon
High volumetric capacitance
High particle density
High-temperature carbonization
Energy storage

ABSTRACT

The inherent low volumetric performance of two-dimensional (2D) carbon materials hinders their practical usage in portable devices. Three-dimensional (3D) carbon materials derived from sustainable biomass have been widely investigated but also suffer from the moderate volumetric performance. In this work, using biomass (jujube) as carbon precursor, robust 3D porous carbon with a high particle density of 1.06 $g\ cm^{-3}$ is synthesized through high-temperature carbonization and subsequent activation. In three-electrode system, the electrode exhibits an ultrahigh volumetric capacitance of 476 $F\ cm^{-3}$ in 6 M KOH electrolyte, which is much higher than previously reported results. The symmetrical two-electrode supercapacitor delivers excellent rate capability (75% capacitance retention at 20 $A\ g^{-1}$) as well as superior cycle stability (91% capacitance retention after 10,000 cycles) in 1 M H_2SO_4 electrolyte. Furthermore, an energy density as high as 13 $Wh\ L^{-1}$ at a power density of 477 $W\ L^{-1}$ is demonstrated in 1 M Li_2SO_4 electrolyte. The high volumetric performance of our biomass-derived porous carbon meets the requirements of portable devices and the fabrication process can be scaled up easily to industrial levels.

* Corresponding author. Nanomaterials Physicochemistry Department, Faculty of Chemical Technology and Engineering, West Pomeranian University of Technology, Szczecin, Piastów Ave. 42, 71-065 Szczecin, Poland.
** Corresponding author.
*** Corresponding author.
E-mail addresses: xchen@zut.edu.pl (X. Chen), paul.chu@cityu.edu.hk (P.K. Chu), ttang@ciac.ac.cn (T. Tang).

https://doi.org/10.1016/j.jpowsour.2018.11.032
Received 16 June 2018; Received in revised form 26 August 2018; Accepted 9 November 2018

1. Introduction

Over the past decades, with the ever-increasing consumption of electricity-based devices especially portable devices, the advanced energy storage systems with high energy density and compact size are highly needed [1]. Supercapacitors, also known as electrochemical capacitors (ECs), have attracted much attention because of their high power density and superior cycle life [2–4]. Until now, various carbon materials including carbon nanotubes, carbon spheres, carbide-derived carbon and graphene have been investigated as electrode materials in ECs [5–11]. Among them, graphene (2D material) possesses favorable features for energy storage such as high electrical conductivity and large specific surface area (SSA) [7,12,13]. However, the inherent problem of 2D materials is poor volumetric performance ($< 50\ F\ cm^{-3}$) arising from the low density (typically lower than $0.5\ g\ cm^{-3}$), which inevitably leads to the increased size of fabricated ECs [14]. And besides, the complicated manufacturing process and high cost further hinder the large-scale implementation of aforementioned materials. The commercial activated carbon (AC) is also limited by low volumetric capacitance (50–80 $F\ cm^{-3}$) and inferior rate capability [14,15]. Therefore, developing economic feasible carbon materials with high volumetric performance and excellent rate capability is imperative to meet the demand of future applications in portable devices.

From a long-term perspective, sustainable biomass can complement or replace traditional carbon precursors, thereby offering great potential for next-generation electrode materials production [16]. The porous carbon materials derived from egg white [17], silk [18], coconut shell [19], soybeans [20] and fungi [21,22] showed remarkable electrochemical performance such as high gravimetric capacitance, good cycling stability and improved rate capability. To obtain biomass-derived carbon materials with enhanced characters for energy storage, KOH activation has been widely utilized to tailor pore characteristics, increase the surface area and introduce functional groups [23–26]. By controlling the weight ratio of KOH/material, hierarchical porous structure, more active sites and high gravimetric capacitance have been achieved [27–30].

However, as a traditional method, low-temperature carbonization combined with subsequent KOH activation is detrimental to the volumetric performance of activated carbon material [31]. The obtained carbonized material produced via low-temperature carbonization of biomass normally possesses the unstable or fragile structure, which will be excessively etched during subsequent KOH activation, resulting in overmuch meso-/macropores and large SSA/pore volume of activated carbon material [32–35]. Although these enhanced characters benefit ions transport and charge accumulation, they severely reduce the particle density and conductivity of activated carbon material, leading to a deterioration in the volumetric performance as well as a higher equivalent series resistance (ESR) of fabricated ECs [36–38]. For instance, various activated carbon materials derived from biomass such as lignin [39], olive pits [40], pomelo peel [31] and soybean residue [36], suffer from a low particle density and exhibit moderate volumetric capacitance (100–150 $F\ cm^{-3}$) [14,41]. In addition, redundant meso-/macropores in carbon structure not only contribute little to capacitance, but also increase the weight of device because of its interior space flooded by electrolyte [41].

Jujube is widely distributed in plains, mountains even deserts in Asia, Africa and southeastern Europe. Herein, conversion of jujube to robust 3D porous carbon through high-temperature carbonization and subsequent KOH activation is described, as illustrated in Scheme 1. The obtained robust 3D porous carbon exhibits a SSA of 829 $m^2\ g^{-1}$ with abundant micropores and some meso-/macropores. Unlike 2D materials with low volumetric performance, the robust 3D porous carbon shows an ultrahigh volumetric capacitance of 476 $F\ cm^{-3}$ due to its high particle density ($1.06\ g\ cm^{-3}$), boding well for portable devices application. The as-fabricated symmetric supercapacitor delivers excellent rate capability (75% capacitance retention at 20 $A\ g^{-1}$) and superior cycle stability (91% capacitance retention after 10,000 cycles) in 1 M H_2SO_4 electrolyte. Moreover, an energy density as high as 13 $Wh\ L^{-1}$ at a power density of 477 $W\ L^{-1}$ is demonstrated in 1 M Li_2SO_4 electrolyte. On account of sustainable raw material, facile synthesis process and outstanding electrochemical performance, the robust 3D porous carbon derived from jujube is a very promising electrode material in portable devices.

2. Experimental

2.1. Synthesis of carbon samples

In a typical synthesis, 6.0 g of commercial freeze-dried Jujube was placed in a ceramic boat and carbonized at high temperature (800 °C, 5 °C min^{-1}) for 2 h under N_2 in a tubular furnace as the initial step. The resulting dark solid was ground to powder. 0.2 g of the high-temperature carbon (HC) was impregnated with 0.4 g, 0.8 g and 1.2 g of KOH (weight KOH/weight HC = 2, 4 and 6) in ethanol, followed by sonication for 10 min and evaporation at 80 °C in oven. Activation was conducted by annealing the mixture at 800 °C for 1 h under N_2 and the sample was washed with 1 M HCl and deionized water. After drying at 90 °C in vacuum for 12 h, the obtained 3D porous high-temperature carbon samples (PHCs) were denoted as PHC-*n*, where *n* is the weight ratio of KOH to HC.

To prove the significant role of high-temperature carbonization in particle density of activated carbon materials, low-temperature carbonization of jujube followed by activation was also investigated as control group. In a typical synthesis, the freeze-dried jujube was firstly carbonized at 500 °C for 2 h in N_2. The resulting low-temperature carbon (LC) was ground to powder and mixed with KOH followed by activation at 800 °C for 1 h under N_2 flow. After purification and drying process, the as-obtained porous low-temperature carbon samples (PLCs) were named as PLC-*x*, where *x* is the weight ratio of KOH to LC.

2.2. Characterization

The morphologies of samples were observed by Field-emission scanning electron microscope (FE-SEM, XL30ESEM-FEG). Transmission electron microscopy (TEM) was performed on the FEI Tecnai F30 transmission electron microscope at 200 kV and X-ray powder diffraction (XRD) was carried out on the Philips diffractometer using Cu K_α radiation. The N_2 adsorption-desorption isotherms were obtained at liquid nitrogen temperature (77 K) using a Micromeritics ASAP 2010M instrument. The Brunauer-Emmett-Teller and density functional theory (DFT) methods were implemented to calculate the SSA and pore size distribution, respectively. The X-ray photoelectron spectroscopy (XPS) spectra was obtained on the XPS-7000 spectrometer (Rigaku) using Mg K_α radiation and Raman spectrum was performed on Renishaw micro-Raman spectrometer (excitation-beam wavelength: 785 nm).

2.3. Electrochemical measurements

Electrochemical measurements of all samples in three-electrode system were conducted on electrochemical workstation (CHI660E, CH Instruments Shanghai). The Pt plate and Hg/HgO electrode were used as counter electrode and reference electrode, respectively. 6 M KOH aqueous solution was used as the electrolyte. The working electrode was prepared by the follow procedures: 80 wt% carbon material, 10 wt % carbon black and 10 wt% poly(tetrafluoroethylene) (PTFE) were mixed in ethanol to form slurry, then coated on the nickel-foam current collector (1 cm × 1 cm) and pressed at a pressure of 10 MPa to form working electrode followed by drying at 90 °C in an oven for 12 h. The mass loading of carbon material on working electrode was ~4 mg. In two-electrode system test, EC-LAB VMP3 (BioLogic Science Instruments) was used. Carbon material, carbon black and PTFE were mixed in ethanol according to the mass ratio of 8:1:1. After drying at

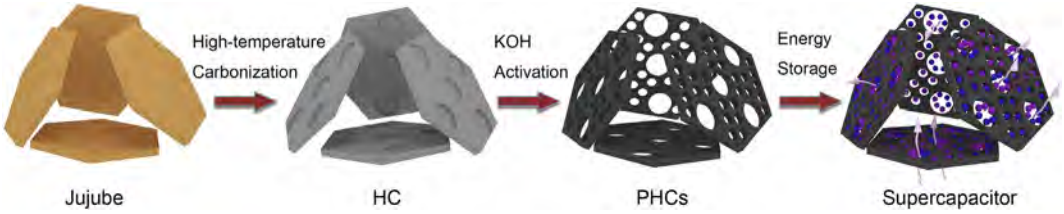

Scheme 1. Schematic illustration of the experimental process for the preparation of robust 3D porous carbon and further energy storage. The small balls represent electrolyte ions and the pink arrows indicate ions transport pathways. (TIFF format, 2 column fitting image).

90 °C in an oven for 12 h, the mixture was pressed at a pressure of 10 MPa to form round electrode with a diameter of 1 cm. The mass loading of carbon material on one electrode was ~4 mg.

In three-electrode system, the gravimetric and volumetric capacitances were calculated from the cyclic voltammetry curves according to [22,42,43]:

$$C_{wt} = \frac{1}{ms(V_b - V_a)} \int_{V_a}^{V_b} I\, dV \quad (1)$$

$$\rho_{particle} = \frac{1}{V_{total} + 1/\rho_{carbon}} \quad (2)$$

$$C_{vol} = C_{wt} * \rho_{particle} \quad (3)$$

where C_{wt} ($F\ g^{-1}$) is gravimetric capacitance, I (A) is the current response, V_b and V_a are the high and low potential limit, V (V) is the potential, m (g) represents the carbon material mass and s ($mV\ s^{-1}$) is the potential scan rate; $\rho_{particle}$ ($g\ cm^{-3}$) is the particle density of carbon material, V_{total} ($cm^3\ g^{-1}$) is the total pore volume of carbon material estimated from N_2 adsorption-desorption isotherm (77 K) and ρ_{carbon} is the true density of carbon material (about 2 $g\ cm^{-3}$) determined by helium density measurements (Table S1); C_{vol} ($F\ cm^{-3}$) is volumetric capacitance, which equals to the product of gravimetric capacitance and particle density of carbon material [22,44].

The specific capacitance, volumetric energy and power densities in two-electrode system were calculated from the charging/discharging profiles by:

$$C = \frac{2I\Delta t}{m\Delta V} \quad (4)$$

$$E_{vol} = E_{wt} * \rho = \frac{C\Delta V^2}{8*3.6} * \rho \quad (5)$$

$$P_{vol} = \frac{3600 * E_{vol}}{\Delta t} \quad (6)$$

where I (A) is the constant discharge current, t (s) is the full discharge time, V (V) represents the voltage change during a full discharge and m (g) is carbon material mass; E_{vol} ($Wh\ L^{-1}$) is the volumetric energy density; P_{vol} ($W\ L^{-1}$) is the volumetric power density.

3. Results and discussion

3.1. Material preparation

Scheme 1 illustrates the preparation process of robust 3D porous jujube-derived carbon and further energy storage. High-temperature carbonization of jujube produces HC with some obstructed or bottlenecked meso-/macropores because of the thermal decomposition of organic components. Subsequent KOH activation is employed to increase the surface area accessible to electrolyte ions by opening these meso-/macropores and introducing abundant micropores. Moreover, KOH activation also modulates the chemical and electronic characteristics of PHCs, further minimizing ions transport resistance [45]. The chemical activation treatment can be described by the following reactions:

$$6KOH + 2C \rightarrow 2K + 3H_2 + 2K_2CO_3 \quad (1)$$

$$K_2CO_3 + C \rightarrow K_2O + 2CO \quad (2)$$

$$K_2CO_3 \rightarrow K_2O + CO_2 \quad (3)$$

$$2K + CO_2 \rightarrow K_2O + CO \quad (4)$$

Usually, hydrothermal method or low-temperature (≤600°C) carbonization is applied in production of biomass derived carbon, which produces unstable or fragile carbon structure. Subsequent KOH activation destroys the carbon skeleton and introduces overmuch meso-/macropores. Despite the large SSA and pore volume, the particle density of these activated carbon materials dramatically decreases [31,40,46,47]. To minimize the detrimental effects, a high carbonization temperature (800 °C) is used here to stabilize the initial carbon skeleton and protect the overall structure from fragmenting during subsequent KOH activation. Meanwhile, the traditional low temperature (500 °C) carbonization followed by KOH activation is also applied as control group.

3.2. Material characterization

The FE-SEM images reveal that KOH activation opens many obstructed or bottlenecked pores in HC (Fig. 1a and d). The overall structure of 3D carbon is almost maintained during activation and the honeycomb-like porous morphology is observed after KOH activation. The stacking graphene layers of HC demonstrate its robust character; after activation, PHC-4 inherits the characteristic robust stacking layers (Fig. 1b and c and Fig. 1e and f). This interesting phenomenon is ascribed to the stable carbon skeleton produced via high-temperature carbonization in this work. Different from 2D carbon materials with a low particle density (< 0.5 $g\ cm^{-3}$), the robust 3D high-temperature porous carbon samples have an ultrahigh particle density (> 1 $g\ cm^{-3}$) (Table S1), which is crucial to the volumetric capacitance of electrodes [20,22]. In contrast, the control group (PLC-4) undergoing low-temperature carbonization and subsequent activation possesses interconnected sheet structure with ubiquitous meso-/macropores (Fig. S1). It suggests that in spite of the same activation conditions, unstable carbon structure produced via low-temperature carbonization is excessively etched during KOH activation process. As a result, low-temperature porous carbon samples exhibit a lower particle density (< 0.7 $g\ cm^{-3}$) (Table S1).

The powder XRD patterns of samples are presented in Fig. 2a. Two broad characteristic peaks at 22° and 43° in the XRD patterns correspond to the (002) and (101) planes of graphitic carbon, respectively. The weak peaks in HC stem from impurities after initial carbonization without washing, especially inorganic compounds derived from trace elements within jujube. As the weight ratio (n) goes up from 2 to 6, the (002) peak shows reduced intensity as a result of more defects introduced by activation. Additionally, the presence of two strong characteristic peaks in PHC-6 also suggests the robust character of carbon structure, although high weight ratio (n = 6) is applied in activation process. In the Raman spectrum (Fig. 2b), the G-band at 1593 cm^{-1} and D-band at 1357 cm^{-1} associate with E_{2g} vibration mode in sp^2-boned graphitic carbons and A_{1g} vibration mode in defective carbon structure,

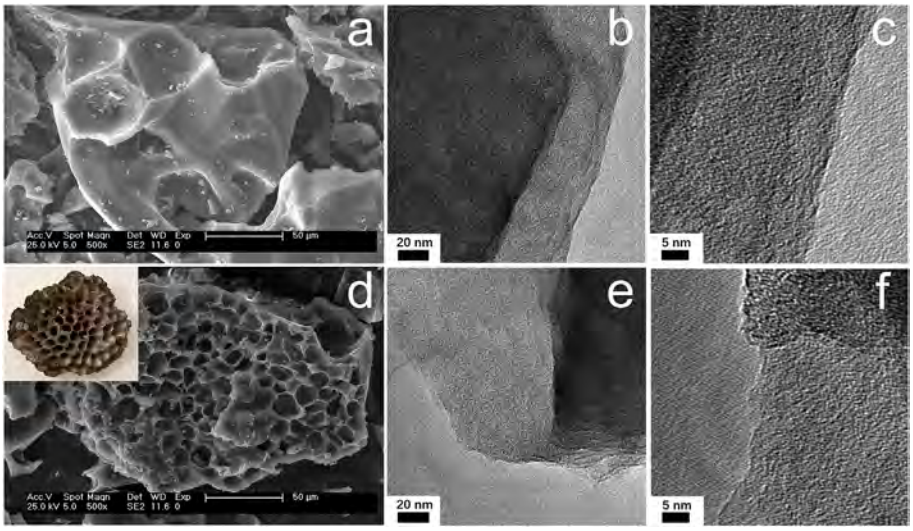

Fig. 1. SEM and TEM images: (a–c) HC and (d–f) PHC-4. (TIFF format, 1.5 column fitting image).

respectively [26]. The intensity ratio of G-band and D-band is used to evaluate the degree of perfection of samples. The progressively lower I_G/I_D ratios from 0.52 of HC to 0.37 of PHC-6 are attributed to more defects as consistent with XRD and SEM results.

XPS is conducted to determine the chemical composition of samples. After carbonization, large amounts of carbon atoms and heteroatoms (primarily O, secondary N) are uniformly distributed on HC and this is the common feature of biomass-derived carbon materials [48]. After activation, only two obvious peaks of carbon (284.6 eV) and oxygen (532.3 eV) are detected, indicating the removal of N elements (Fig. S2). The high-resolution C 1s XPS spectra (Fig. 2c and d, Fig. S3) is fitted by four sub-peaks: graphitic carbon (284.4–284.6 eV), −C−OH (285.6–285.7eV), −CO (286.7–287.0 eV), and −COOH (288.7–289.0 eV). Notably, PHC-4 possesses more oxygen-containing surface functional groups (−C−OH and −CO) in comparison with HC, indicating partial conversion of carbon atoms within the graphitic structure (−C-C−) and carboxyl groups (−COOH) into −C−OH or −-CO functional groups during activation process. These increased active sites are beneficial for charge accumulation and ions transport in assembled ECs [15].

The N_2 adsorption-desorption isotherms are acquired to investigate the effect of various weight ratios of KOH/HC (n) on porosity of samples (Fig. 3a). As n increases from 2 to 6, the SSA initially increases from 656 $m^2\ g^{-1}$ for PHC-2 to 829 $m^2\ g^{-1}$ for PHC-4 and then decreases to 783 $m^2\ g^{-1}$ for PHC-6 as calculated by the Brunauer-Emmett-Teller method. The negligible adsorption value within the P/P_0 range of 0–0.1 in type III isotherms implies nondetectable micropores in HC. The typical I/IV type curves with the H4 hysteresis loop of PHCs indicate the presence of abundant micropores and some meso-/macropores; which is probed by dramatically increased adsorption values within the low relative pressure range (P/P_0 = 0–0.1) with moderate increased adsorption values within the high relative pressure range (P/P_0 = 0.5–1.0). The hierarchical porous structure of PHCs including micro- and meso-/macropores not only benefit charge accumulation via the formation of

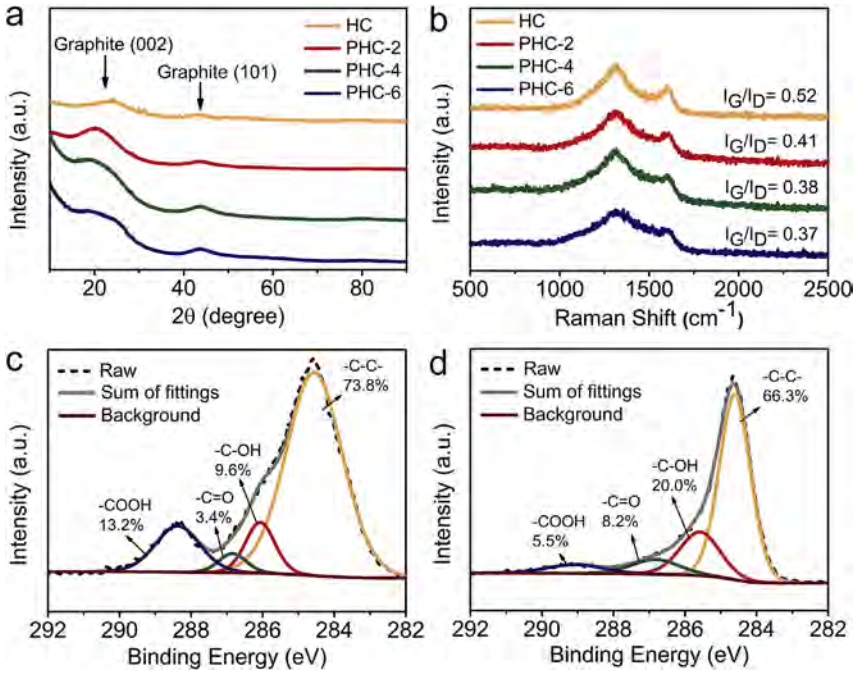

Fig. 2. (a) XRD patterns and (b) Raman spectrum of samples; High-resolution C 1s XPS spectra of HC (c) and PHC-4 (d). (TIFF format, 1 column fitting image).

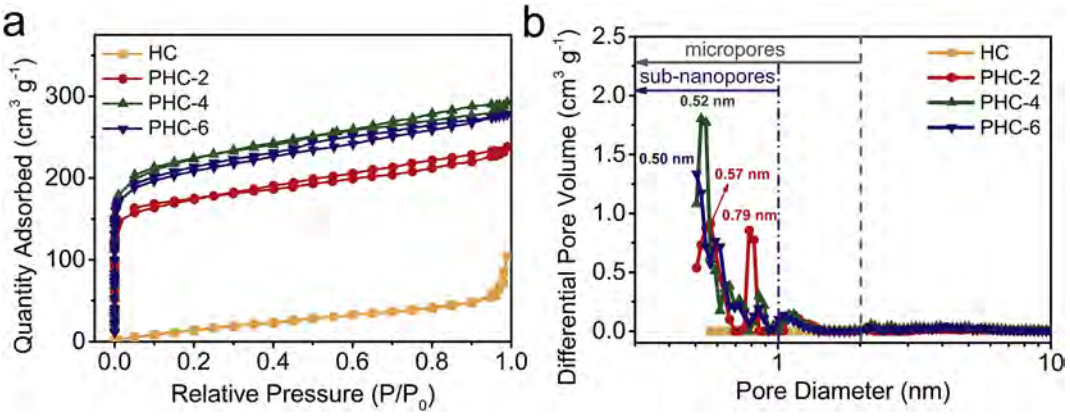

Fig. 3. (a) N_2 adsorption-desorption isotherms and (b) Pore size distributions of samples. (TIFF format, 1 column fitting image).

electrical double layer but also provide pathways for electrolyte ions diffusion [18,49].

The pore size distributions are estimated by density functional theory (DFT) method (Fig. 3b). The pores of PHCs are mainly micropores (< 2 nm), especially the emerging sub-nanopores smaller than 1 nm in comparison with HC (Table 1). These sub-nanopores will play a prominent role in the enhanced capacitance, as revealed by previous studies on charge storage mechanism [5,50]. Furthermore, activation process of HC significantly contributes to the formation of micropores but does not introduce overmuch meso-/macropores (Fig. S4, Table 1). As mentioned above, this phenomenon is attributed to the robust structure that prevents the immoderate thermal reduction reaction between HC and KOH.

The effect of various carbonization temperatures followed by activation on particle density of activated carbon materials is further studied from the perspective of total pore volume. High-temperature (800 °C) carbonization followed by KOH activation produces PHCs with slightly increased total pore volume as well as moderately reduced particle density (Fig. 4a). PHCs have small pore volume from 0.37 to 0.45 $cm^3\ g^{-1}$, resulting in the high particle density (> 1 g cm^{-3}). For instance, PHC-4 has a small pore volume of 0.45 $cm^3\ g^{-1}$ and a high particle density of 1.06 $g\ cm^{-3}$ (Table S1). In sharp contrast, the low-temperature (500 °C) carbonization followed by KOH activation produces PLCs with ultrahigh SSA in excess of 2000–3000 $m^2\ g^{-1}$ (Table S2), which clearly demonstrates the excessive activation process. Notably, the large pore volume of PLCs (1.11–2.34 $cm^3\ g^{-1}$) are several times higher than that of PHCs, indicating the significant decrease of particle density (< 0.7 g cm^{-3}) (Fig. 4b). For instance, PLC-4 has a large pore volume of 1.70 $cm^3\ g^{-1}$ and a low particle density of 0.46 $g\ cm^{-3}$ (Table S1). That is, the high-temperature and low-temperature carbonization followed by KOH activation process determine the high and low particle densities of activated carbon materials, respectively. And besides, from the perspective of SSA [22], aforementioned relationship is also verified (Fig. S5).

3.3. Electrochemical performance

Based on above analysis, PHCs with more active sites, abundant micropores, high particle density and hierarchical porous structure are expected to deliver high volumetric performance. We study the electrochemical performance of samples in three-electrode system using 6 M KOH electrolyte. Fig. 5a–b illustrate the cyclic voltammetry curves of all samples at 20 $mV\ s^{-1}$ and cyclic voltammetry curves of PHC-4 at various scan rates from 1 to 100 $mV\ s^{-1}$. PHCs exhibit the increased gravimetric capacitance in comparison with HC. Among them, PHC-4 exhibits a highest gravimetric capacitance of 449 $F\ g^{-1}$ at a scan rate of 1 $mV\ s^{-1}$ (Fig. S6).

Although graphene (2D material) has a high gravimetric capacitance, its low particle density leads to the poor volumetric performance [41]. Many 3D carbon materials also suffer from a low particle density and moderate volumetric performance [36,39,40]. For instance, using same biomass (jujube) as precursor without high-temperature carbonization process [51], Sun et al. have reported a high gravimetric capacitance of 398 $F\ g^{-1}$ but a low volumetric capacitance of 96 $F\ cm^{-3}$. Therefore, it is difficult to optimize the electrodes with high gravimetric capacitance as well as high volumetric capacitance. Whereas, based on a high particle density (1.06 $g\ cm^{-3}$), the volumetric capacitance of PHC-4 is calculated to be 476, 410, 382, 352, 284 and 206 $F\ cm^{-3}$ (Fig. 5c) at a scan rate of 1, 5, 10, 20, 50 and 100 $mV\ s^{-1}$, respectively. As illustrated in Fig. 5d, the volumetric capacitance of PHC-4 is higher than that of many biomass-derived carbon materials including auricularia [22], kraft pulp [52], perilla frutescens [53], corn straw [54], elm samara [48], seaweeds [55] and kelp [56], even higher than high-density graphene materials [43,57] (Table S3).

Table 1
Physical porosity parameters for samples.

Sample	S_{BET}(m^2 g^{-1})[a]	S_{DFT}(m^2 g^{-1})[b]	S_{micro}(m^2 g^{-1})[c]	Vt ($cm^3\ g^{-1}$)[d]	Pore vol ($cm^3\ g^{-1}$)[e]				PSDFT (nm)[f]
					V_t^{DFT}	$V_{<1\,nm}$	$V_{1-2\,nm}$	$V_{>2\,nm}$	
HC	64	39	3.3 (8%)	0.16	0.09	0.00	0.00	0.09	2.38
PHC-2	656	811	749 (92%)	0.37	0.33	0.20	0.03	0.10	0.57
PHC-4	829	1002	860 (86%)	0.45	0.42	0.23	0.03	0.16	0.52
PHC-6	783	956	837 (88%)	0.43	0.40	0.22	0.03	0.15	0.50

[a] Brunaur-Emmett-Teller method is used to calculate the specific surface area.
[b] Density functional theory (DFT) method is used to calculate the specific surface area.
[c] The surface area of micropores is calculated based on DFT analysis. Numbers in brackets denote the percentage share in the S_{DFT}.
[d] The total pore volume is determined at a relative pressure of 0.98.
[e] The volume of total pores, pores smaller than 1 nm, pores between 1 and 2 nm and pores bigger than 2 nm is obtained from DFT analysis.
[f] The Pore size is obtained by DFT analysis.

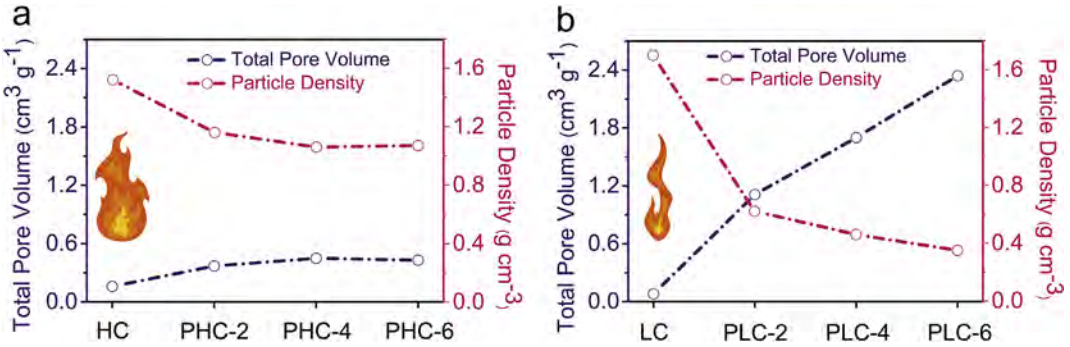

Fig. 4. (a) Effect of high-temperature carbonization followed by activation on total pore volume and particle density. (b) Effect of low-temperature carbonization followed by activation on total pore volume and particle density. (TIFF format, 1 column fitting image).

Previous report has revealed that the capacitance is not dependent on the SSA and pore volume, but the surface area accessible to electrolyte ions and carbon structure [48]. For instance, the egg-box-like carbon with a high SSA (2312 $m^2\ g^{-1}$) exhibits a low volumetric capacitance of 27 $F\ cm^{-3}$ [58], whereas the 3D porous layer-stacking carbon with a SSA of 1103 $m^2\ g^{-1}$ has a high capacitance of 360 $F\ cm^{-3}$ [22]. It is totally consistent with our results, where the volumetric capacitance of PHC-4 is as high as 476 $F\ cm^{-3}$ with moderate SSA of 829 $m^2\ g^{-1}$. A possible interpretation about the high volumetric capacitance of PHC-4 is proposed. The robust structure of high-temperature carbon is stable enough to undergo activation process, which produces a hierarchical porous structure of PHC-4 without sacrificing the high particle density. Some meso-/macropores in the 3D porous structure serve as pathways for electrolyte ions diffusion and functional groups on the surface facilitate the ions transfer. Thus, electrolyte ions can access to abundant micropores in the structure, which leads to the superior volumetric capacitance.

The capacitive behaviors of samples are also confirmed in two-electrode system using 1 M H_2SO_4 electrolyte. The roughly rectangular CV curves at 100 $mV\ s^{-1}$ of PHCs can be attributed to the 3D porous structure ensuring effective transport of electrolyte ions throughout the electrodes (Fig. 6a). Fig. 6b shows the superior triangular charging/discharging curves of PHCs. At a low current density of 1 $A\ g^{-1}$, a high specific capacitance of 158 $F\ g^{-1}$ is obtained for PHC-4 and it is higher than that of commercial AC ($< 100\ F\ g^{-1}$) [4]. At a high current density of 20 $A\ g^{-1}$, PHC-4 still retains 75% of its initial capacitance (118 $F\ g^{-1}$), revealing the excellent rate capability (Fig. 6c). Moreover, the PHC-4 based EC shows 91% capacitance retention over 10,000 charging/discharging cycles at a current density of 10 $A\ g^{-1}$ (Fig. 6d). A comparison of 1st and 10000th cycle curves (inset) further verifies the superior cycle stability in energy storage.

To further understand the enhanced capacitance and excellent rate

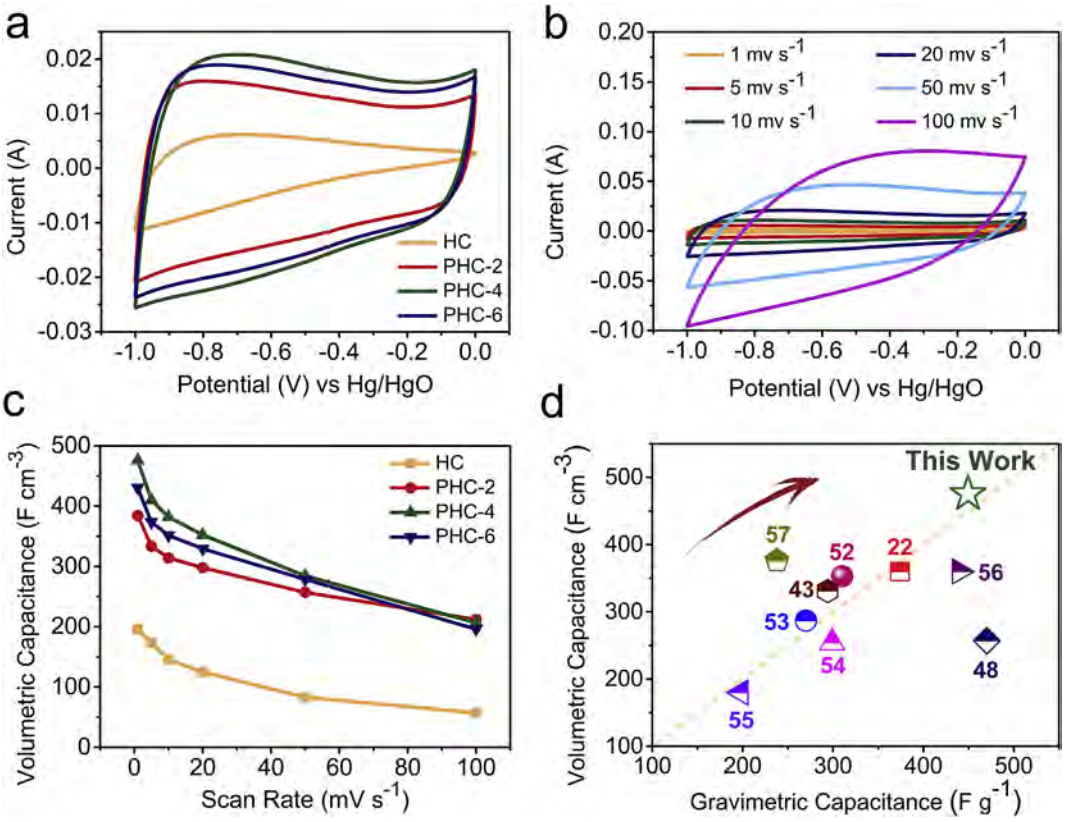

Fig. 5. Electrochemical performance of samples in three-electrode system using aqueous 6 M KOH electrolyte: (a) CV curves at a scan rate of 20 $mV\ s^{-1}$; (b) CV curves of PHC-4 electrode at various scan rates; (c) Comparison of volumetric capacitance at various scan rates; (d) Comparison of volumetric and gravimetric capacitances of PHC-4 electrode with other carbon electrodes in aqueous electrolytes. (TIFF format, 1.5 column fitting image).

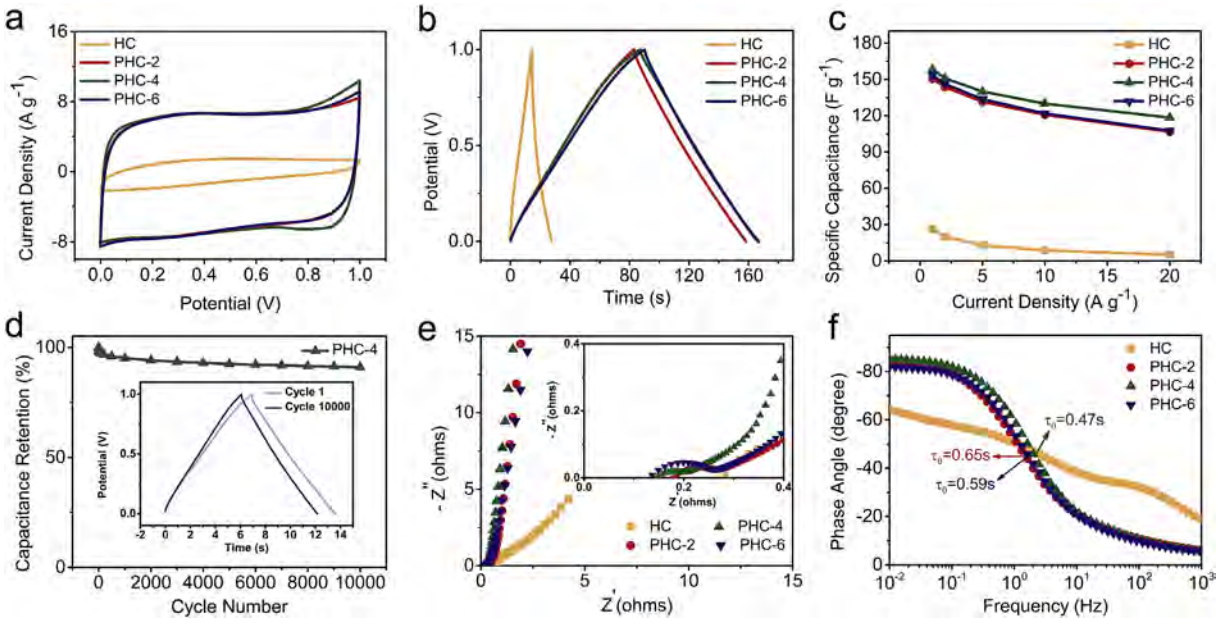

Fig. 6. Electrochemical performance of samples in two-electrode system in aqueous 1 M H_2SO_4: (a) CV curves at a scan rate of 100 $mV\ s^{-1}$; (b) Galvanostatic charging/discharging curves at a current density of 1 $A\ g^{-1}$; (c) Comparison of specific capacitance at various current densities; (d) Cycling stability of PHC-4 at a current density of 10 $A\ g^{-1}$. The inset shows the first and last charging/discharging curves of PHC-4; (e) Nyquist plots and (f) Impedance phase angle versus frequency. (TIFF format, 2 column fitting image).

capability of PHC-4, we carry out electrochemical impedance spectroscopy (EIS) studies. The Nyquist plot based on the impedance data is shown in Fig. 6e. The vertical curves of PHCs at low frequencies indicate superior capacitive behaviors. The expanded view at high frequencies illustrates the shortest 45° Warburg region followed by the smallest semicircle for PHC-4, indicating the shortest electrolyte diffusion pathways and efficient charge transfer [59]. Notably, the lower ESR is ascribed to optimized electrodes with lower ions diffusion resistance as well as lower electrical resistance [60]. The ESR is measured to be 0.35 Ω for PHC-4 by expanding the vertical part of the plot to the Z′ axis, much lower than other biomass-derived materials [61–63]. The dependence of the phase angle on frequency is shown in Fig. 6f. The phase angles of PHCs are close to -90° at low frequencies, suggesting the ideal capacitive behaviors. In contrast, HC exhibits an inferior frequency response with a phase angle of -65°. When the phase angle reaches to -45°, the corresponding characteristic frequency f_0 marks the point where the resistive and capacitive impedances are equal [64]. PHC-2, PHC-4 and PHC-6 show f_0 of 1.54 Hz, 2.13 Hz, and 1.69 Hz, respectively. The corresponding time constant τ_0 ($\tau_0 = 1/f_0$) of PHC-4 is 0.47s, which is lower than that of two others and much better than 10 s of conventional activated carbon-based ECs [7].

Because energy density is proportional to the square of voltage window, the neutral aqueous electrolyte of 1 M Li_2SO_4 is also applied in symmetric supercapacitor because of its wide working voltage window (Fig. 7a, Fig. S7a). Fig. 7b displays the CV curves of the symmetric supercapacitor at various voltage windows. The higher voltage window of 0–2.2 V has been reported for activated carbon based symmetric supercapacitor in 1 M Li_2SO_4 electrolyte [65]. In this work, the initial sharp increase of anodic current of CV curve at 0–2.0 V is observed while no obvious increase is detected at 0–1.8 V. The stable voltage window of 0–1.8 V in neutral Li_2SO_4 electrolyte is attributed to the low H^+/OH^- concentration as well as the oxygen-containing functional groups in the carbon structure, leading to the high oxygen or hydrogen evolution potential [22].

The rectangular-like shape of CV curve at voltage window of 0–1.8 V at a high scan rate of 100 $mV\ s^{-1}$ indicates the excellent rate performance (Fig. 7c), further demonstrated by the nearly triangle shape of galvanostatic charge/discharge curves at various current densities (Fig. 7d). Importantly, the volumetric energy and power densities are used to evaluate the electrochemical performance of symmetrical supercapacitor. The assembled PHC-4 based symmetric supercapacitor exhibits a high volumetric energy density of 13 $Wh\ L^{-1}$ at a power density of 477 $W\ L^{-1}$ (Fig. 7e), almost three times higher than that of commercial supercapacitors (4 ~ 5 $Wh\ L^{-1}$). The calculated energy density is also higher than that of previously reported biomass derived carbon-based symmetric supercapacitors, such as corn straw derived carbon (11.1 $Wh\ L^{-1}$) [54], seaweed-derived carbon (6.7 $Wh\ L^{-1}$) [55], silk cocoon-derived carbon (5.2 $Wh\ L^{-1}$) [66], bagasse-derived carbon (10.9 $Wh\ L^{-1}$) [67] and moringa oleifera derived carbon (11.8 $Wh\ L^{-1}$) [58], even higher than densely graphene sheets (7.4 $Wh\ L^{-1}$) [68]. Furthermore, using single PHC-4 based symmetric supercapacitor, we successfully light the red LED (Fig. 7f) and yellow LED (Fig. S7b), which is a visual exhibition of practical usage on energy storage.

4. Conclusions

Robust 3D porous carbon is produced from low-cost biomass (jujube) through high-temperature carbonization and subsequent KOH activation. Due to its high particle density (1.06 $g\ cm^{-3}$), more active sites, abundant micropores and hierarchical porous structure, the as-obtained robust 3D porous carbon exhibits a volumetric capacitance as high as 476 $F\ cm^{-3}$ in three-electrode system in 6 M KOH, which is super to that of other biomass-derived carbon materials. The excellent rate capability (75% capacitance retention at 20 $A\ g^{-1}$) and superior cycle life (91% capacitance retention after 10,000 cycles) are demonstrated in 1 M H_2SO_4 in two-electrode system. The PHC-4 based symmetric supercapacitor delivers a high volumetric energy density of 13 $Wh\ L^{-1}$ in 1 M Li_2SO_4 under a wide voltage window of 0–1.8 V. This work opens up feasible approach for the production of biomass-derived electrode materials with promising application in portable devices.

Conflicts of interest

There are no conflicts of interest to declare.

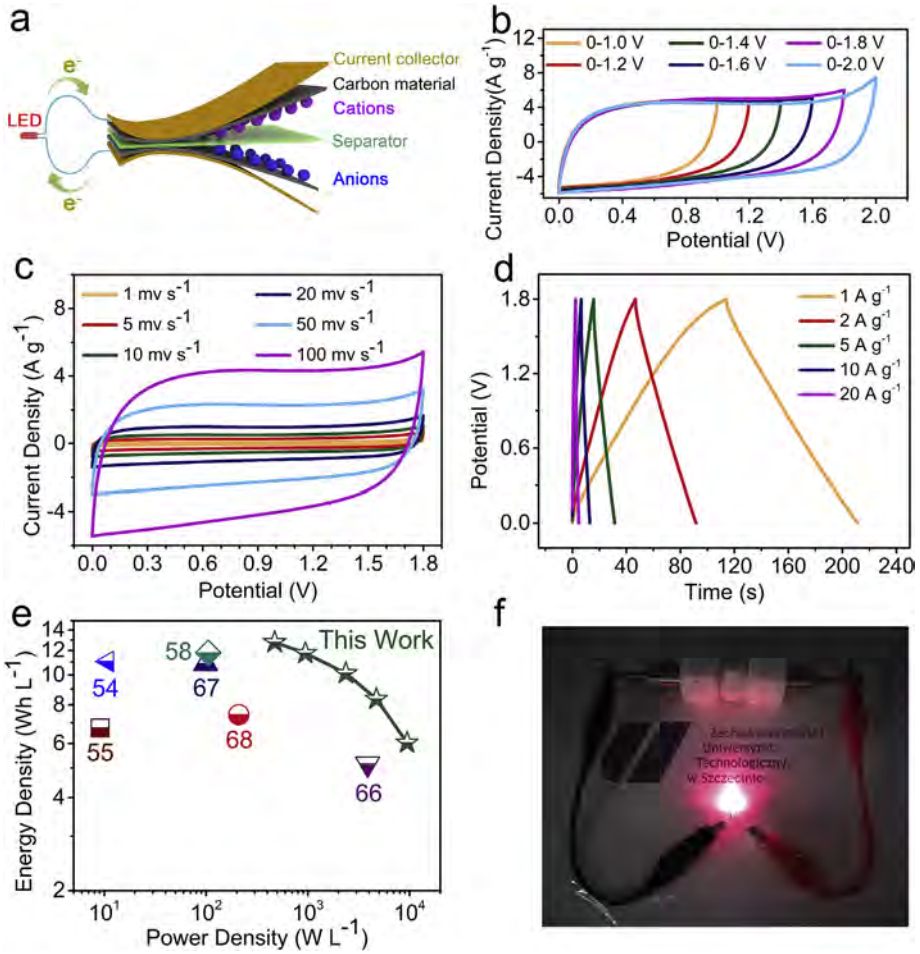

Fig. 7. Electrochemical performance of PHC-4 in aqueous 1 M Li_2SO_4: (a) Schematic of assembled symmetric supercapacitor. (b) CV curves at a scan rate of 100 $mV\ s^{-1}$ under various voltage windows; (c) CV curves under various scan rates; (d) Galvanostatic charging/discharging curves under various current densities; (e) Ragone plot of PHC-4 and other carbon-based symmetric supercapacitors in aqueous electrolytes; (f) Photograph of red LED powered by PHC-4 based supercapacitor. (TIFF format, 1.5 column fitting image). (For interpretation of the references to colour in this figure legend, the reader is referred to the Web version of this article.)

Declarations of interest

None.

Acknowledgements

This work was financially supported by National Science Centre, Poland within UMO-2015/18/E/ST8/00291, Hong Kong Innovation and Technology Fund (ITF) ITS/452/17FP, and Hong Kong Research Grants Council (RGC) General Research Funds (GRF) Nos. CityU 11301215 and 1120561.

Appendix A. Supplementary data

Supplementary data to this article can be found online at https://doi.org/10.1016/j.jpowsour.2018.11.032.

References

[1] N. Armaroli, V. Balzani, Energy Environ. Sci. 4 (2011) 3193–3222.
[2] B.E. Conway, Kluwer, Dordrecht, the Netherland, (1999).
[3] J.R. Miller, P. Simon, Science 321 (2008) 651–652.
[4] P. Simon, Y. Gogotsi, Nat. Mater. 7 (2008) 845–854.
[5] J. Chmiola, G. Yushin, Y. Gogotsi, C. Portet, P. Simon, P.L. Taberna, Science 313 (2006) 1760–1763.
[6] M. Kaempgen, C.K. Chan, J. Ma, Y. Cui, G. Gruner, Nano Lett. 9 (2009) 1872–1876.
[7] M.F. El-Kady, V. Strong, S. Dubin, R.B. Kaner, Science 335 (2012) 1326–1330.
[8] N.A. Kumar, H.-J. Choi, Y.R. Shin, D.W. Chang, L. Dai, J.-B. Baek, ACS Nano 6 (2012) 1715–1723.
[9] S.H. Aboutalebi, A.T. Chidembo, M. Salari, K. Konstantinov, D. Wexler, H.K. Liu, S.X. Dou, Energy Environ. Sci. 4 (2011) 1855–1865.
[10] L.J. Yan, D. Li, T.T. Yan, G.R. Chen, L.Y. Shi, Z.X. An, D.S. Zhang, ACS Sustain. Chem. Eng. 6 (2018) 5265–5272.
[11] H. Wang, T.T. Yan, L.Y. Shi, G.R. Chen, J.P. Zhang, D.S. Zhang, ACS Sustain. Chem. Eng. 5 (2017) 3329–3338.
[12] Y.X. Xu, Z.Y. Lin, X. Zhong, X.Q. Huang, N.O. Weiss, Y. Huang, X.F. Duan, Nat. Commun. 5 (2014).
[13] H.Y. Duan, T.T. Yan, G.R. Chen, J.P. Zhang, L.Y. Shi, D.S. Zhang, Chem. Commun. 53 (2017) 7465–7468.
[14] P. Simon, Y. Gogotsi, Accounts Chem. Res. 46 (2013) 1094–1103.
[15] L. Wei, M. Sevilla, A.B. Fuertes, R. Mokaya, G. Yushin, Adv. Energy Mater. 1 (2011) 356–361.
[16] S. Dutta, A. Bhaumik, K.C.-W. Wu, Energy Environ. Sci. 7 (2014) 3574–3592.
[17] Z. Li, Z. Xu, X. Tan, H. Wang, C.M. Holt, T. Stephenson, B.C. Olsen, D. Mitlin, Energy Environ. Sci. 6 (2013) 871–878.
[18] J. Hou, C. Cao, F. Idrees, X. Ma, ACS Nano 9 (2015) 2556–2564.
[19] D. Hulicova-Jurcakova, M. Seredych, G.Q. Lu, T.J. Bandosz, Adv. Funct. Mater. 19 (2009) 438–447.
[20] C. Long, L. Jiang, X. Wu, Y. Jiang, D. Yang, C. Wang, T. Wei, Z. Fan, Carbon 93 (2015) 412–420.
[21] P. Cheng, S. Gao, P. Zang, X. Yang, Y. Bai, H. Xu, Z. Liu, Z. Lei, Carbon 93 (2015) 315–324.
[22] C. Long, X. Chen, L. Jiang, L. Zhi, Z. Fan, Nanomater. Energy 12 (2015) 141–151.
[23] M. Sevilla, W. Gu, C. Falco, M.-M. Titirici, A. Fuertes, G. Yushin, J. Power Sources 267 (2014) 26–32.
[24] L. Xie, G. Sun, F. Su, X. Guo, Q. Kong, X. Li, X. Huang, L. Wan, K. Li, C. Lv, J. Mater. Chem. 4 (2016) 1637–1646.
[25] Y.-Q. Zhao, M. Lu, P.-Y. Tao, Y.-J. Zhang, X.-T. Gong, Z. Yang, G.-Q. Zhang, H.-L. Li, J. Power Sources 307 (2016) 391–400.
[26] W. Qian, F. Sun, Y. Xu, L. Qiu, C. Liu, S. Wang, F. Yan, Energy Environ. Sci. 7 (2014) 379–386.
[27] Y. Zhu, S. Murali, M.D. Stoller, K. Ganesh, W. Cai, P.J. Ferreira, A. Pirkle,

R.M. Wallace, K.A. Cychosz, M. Thommes, Science 332 (2011) 1537–1541.
[28] R. Zeng, X.N. Tang, B.Y. Huang, K. Yuan, Y.W. Chen, Chemelectrochem 5 (2018) 515–522.
[29] M. Sevilla, A.B. Fuertes, Energy Environ. Sci. 4 (2011) 1765–1771.
[30] M. Sevilla, A.B. Fuertes, R. Mokaya, Energy Environ. Sci. 4 (2011) 1400–1410.
[31] G.S. Fu, Q. Li, J.L. Ye, J.J. Han, J.Q. Wang, L. Zhai, Y.W. Zhu, J. Mater. Sci. Mater. Electron. 29 (2018) 7707–7717.
[32] J. Zhou, L. Bao, S.J. Wu, W. Yang, H. Wang, Carbohydr. Polym. 173 (2017) 321–329.
[33] N. Konikkara, L.J. Kennedy, J.J. Vijaya, J. Hazard Mater. 318 (2016) 173–185.
[34] K. Wang, R. Yan, N. Zhao, X.D. Tian, X. Li, S.W. Lei, Y. Song, Q.G. Guo, L. Liu, Mater. Lett. 174 (2016) 249–252.
[35] L. Qie, W.M. Chen, H.H. Xu, X.Q. Xiong, Y. Jiang, F. Zou, X.L. Hu, Y. Xin, Z.L. Zhang, Y.H. Huang, Energy Environ. Sci. 6 (2013) 2497–2504.
[36] G.A. Ferrero, A.B. Fuertes, M. Sevilla, Sci. Rep. UK 5 (2015).
[37] J.T. Sun, J. Niu, M.Y. Liu, J. Ji, M.L. Dou, F. Wang, Appl. Surf. Sci. 427 (2018) 807–813.
[38] C.Z. Zhan, X.L. Yu, Q.H. Liang, W. Liu, Y.B. Wang, R.T. Lv, Z.H. Huang, F.Y. Kang, RSC Adv. 6 (2016) 89391–89396.
[39] H. Li, D. Yuan, C.H. Tang, S.X. Wang, J.T. Sun, Z.B. Li, T. Tang, F.K. Wang, H. Gong, C.B. He, Carbon 100 (2016) 151–157.
[40] E. Redondo, J. Carretero-Gonzalez, E. Goikolea, J. Segalini, R. Mysyk, Electrochim. Acta 160 (2015) 178–184.
[41] Y. Gogotsi, P. Simon, Science 334 (2011) 917–918.
[42] Y.M. Li, D. Zhao, Chem. Commun. 51 (2015) 5598–5601.
[43] Y. Tao, X.Y. Xie, W. Lv, D.M. Tang, D.B. Kong, Z.H. Huang, H. Nishihara, T. Ishii, B.H. Li, D. Golberg, F.Y. Kang, T. Kyotani, Q.H. Yang, Sci. Rep. UK 3 (2013).
[44] H. Itoi, H. Nishihara, T. Kogure, T. Kyotani, J. Am. Chem. Soc. 133 (2011) 1165–1167.
[45] J.C. Wang, S. Kaskel, J. Mater. Chem. 22 (2012) 23710–23725.
[46] Y. Wang, R. Yang, M. Li, Z.J. Zhao, Ind. Crop. Prod. 65 (2015) 216–226.
[47] Z.P. Qiu, Y.S. Wang, X. Bi, T. Zhou, J. Zhou, J.P. Zhao, Z.C. Miao, W.M. Yi, P. Fu, S.P. Zhuo, J. Power Sources 376 (2018) 82–90.
[48] C. Chen, D.F. Yu, G.Y. Zhao, B.S. Du, W. Tang, L. Sun, Y. Sun, F. Besenbacher, M. Yu, Nanomater. Energy 27 (2016) 377–389.
[49] S.S. Zhao, T.T. Yan, H. Wang, J.P. Zhang, L.Y. Shi, D.S. Zhang, ACS Appl. Mater. Interfaces 8 (2016) 18027–18035.
[50] J. Chmiola, C. Largeot, P.L. Taberna, P. Simon, Y. Gogotsi, Angew. Chem. Int. Ed. 47 (2008) 3392–3395.
[51] K.L. Sun, S.S. Yu, Z.L. Hu, Z.H. Li, G.T. Lei, Q.Z. Xiao, Y.H. Ding, Electrochim. Acta 231 (2017) 417–428.
[52] R.J. Mo, Y. Zhao, M.M. Zhao, M. Wu, C. Wang, J.P. Li, S. Kuga, Y. Huang, Chem. Eng. J. 346 (2018) 104–112.
[53] B. Liu, Y.J. Liu, H.B. Chen, M. Yang, H.M. Li, J. Power Sources 341 (2017) 309–317.
[54] Q.X. Xie, R.R. Bao, A.R. Zheng, Y.F. Zhang, S.H. Wu, C. Xie, P. Zhao, ACS Sustain. Chem. Eng. 4 (2016) 1422–1430.
[55] E. Raymundo-Pinero, F. Leroux, F. Beguin, Adv. Mater. 18 (2006) 1877-+.
[56] J. Li, K. Liu, X. Gao, B. Yao, K.F. Huo, Y.L. Cheng, X.F. Cheng, D.C. Chen, B. Wang, W.M. Sun, D. Ding, M.L. Liu, L. Huang, ACS Appl. Mater. Interfaces 7 (2015) 24622–24628.
[57] L.L. Jiang, L.Z. Sheng, C.L. Long, Z.J. Fan, Nanomater. Energy 11 (2015) 471–480.
[58] Y.J. Cai, Y. Luo, Y. Xiao, X. Zhao, Y. Liang, H. Hu, H.W. Dong, L.Y. Sun, Y.L. Liu, M.T. Zheng, ACS Appl. Mater. Interfaces 8 (2016) 33060–33071.
[59] G.P. Wang, L. Zhang, J.J. Zhang, Chem. Soc. Rev. 41 (2012) 797–828.
[60] L.L. Zhang, X. Zhao, Chem. Soc. Rev. 38 (2009) 2520–2531.
[61] N.H. Basri, M. Deraman, S. Kanwal, I.A. Talib, J.G. Manjunatha, A.A. Aziz, R. Farma, Biomass Bioenergy 59 (2013) 370–379.
[62] G.Y. Zhao, C. Chen, D.F. Yu, L. Sun, C.H. Yang, H. Zhang, Y. Sun, F. Besenbacher, M. Yu, Nanomater. Energy 47 (2018) 547–555.
[63] Y.H. Shi, L.L. Zhang, T.B. Schon, H.H. Li, C.Y. Fan, X.Y. Li, H.F. Wang, X.L. Wu, H.M. Xie, H.Z. Sun, D.S. Seferos, J.P. Zhang, ACS Appl. Mater. Interfaces 9 (2017) 42699–42707.
[64] P. Taberna, P. Simon, J.-F. Fauvarque, J. Electrochem. Soc. 150 (2003) A292–A300.
[65] K. Fic, G. Lota, M. Meller, E. Frackowiak, Energy Environ. Sci. 5 (2012) 5842–5850.
[66] C. Long, J.L. Zhuang, Y. Xiao, M.T. Zheng, H. Hu, H.W. Dong, B.F. Lei, H.R. Zhang, Y.L. Liu, J. Power Sources 310 (2016) 145–153.
[67] H.B. Feng, H. Hu, H.W. Dong, Y. Xiao, Y.J. Cai, B.F. Lei, Y.L. Liu, M.T. Zheng, J. Power Sources 302 (2016) 164–173.
[68] Y. Yoon, K. Lee, S. Kwon, S. Seo, H. Yoo, S. Kim, Y. Shin, Y. Park, D. Kim, J.Y. Choi, H. Lee, ACS Nano 8 (2014) 4580–4590.

Supporting information

Biomass-Derived Robust Three-Dimensional Porous Carbon for High Volumetric Performance Supercapacitors

Xiaoguang Liu,[a] Changde Ma,[b] Jiaxin Li,[b] Beata Zielinska,[a] Xuecheng Chen,[a,b]* Paul K. Chu,[c]* Tao Tang,[b]* Ewa Mijowska[a]

[a] Nanomaterials Physicochemistry Department, West Pomeranian University of Technology Szczecin, al. Piastów 45, 70-311 Szczecin, Poland

[b] State Key Laboratory of Polymer Physics and Chemistry, Changchun Institute of Applied Chemistry, Chinese Academy of Sciences (CAS), Renmin Street 5625, Changchun 130022, China

[c.] Department of Physics and Department of Materials Science and Engineering, City University of Hong Kong, Tat Chee Avenue, Kowloon, Hong Kong, China

*Corresponding authors: xchen@zut.edu.pl (X. C. Chen); paul.chu@cityu.edu.hk (P. K. Chu); ttang@ciac.ac.cn (T. Tang)

Fig. S1. SEM and TEM of PLC-4.

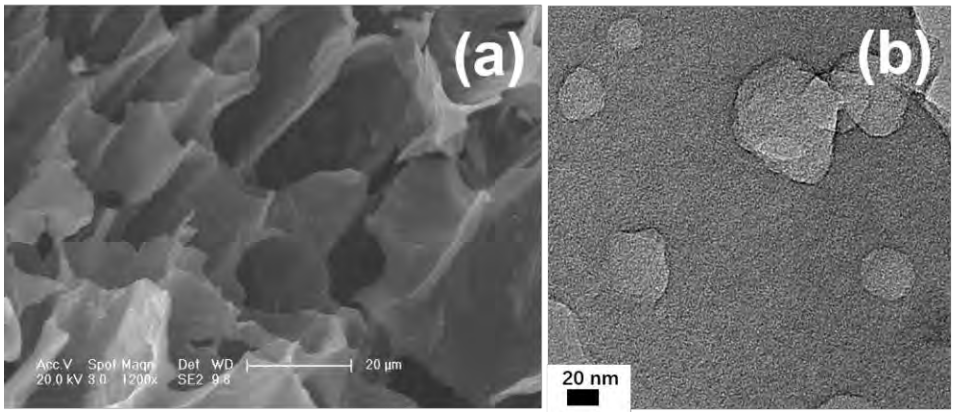

Fig. S2. XPS spectra of HC, PHC-2, PHC-4, and PHC-6.

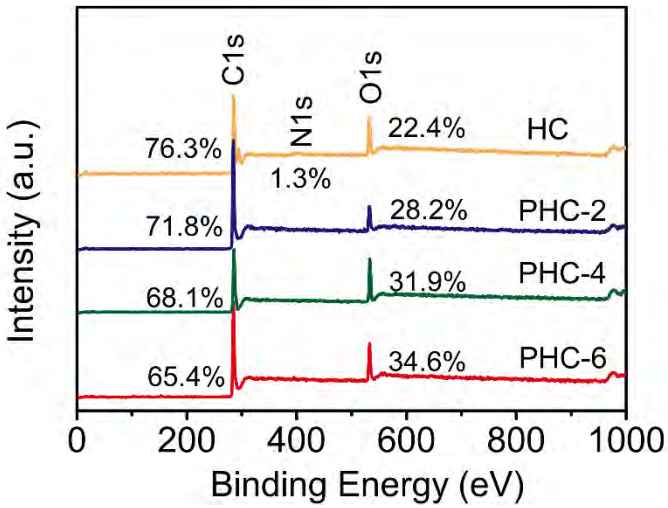

Fig. S3. High-resolution C 1s XPS spectra of PHC-2 (a) and PHC-6 (b).

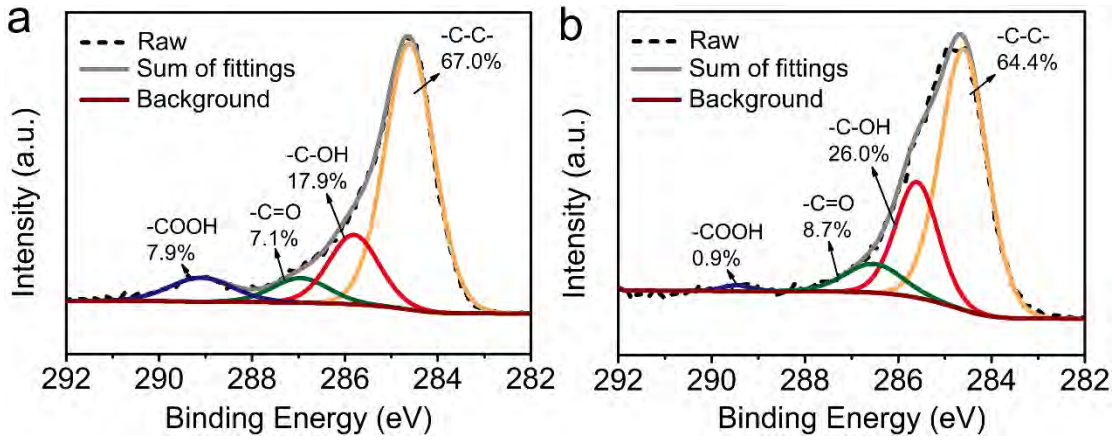

Fig. S4. Effect of activation process on (a) specific surface area and (b) total pore volume of PHCs. Data used here is calculated from DFT method.

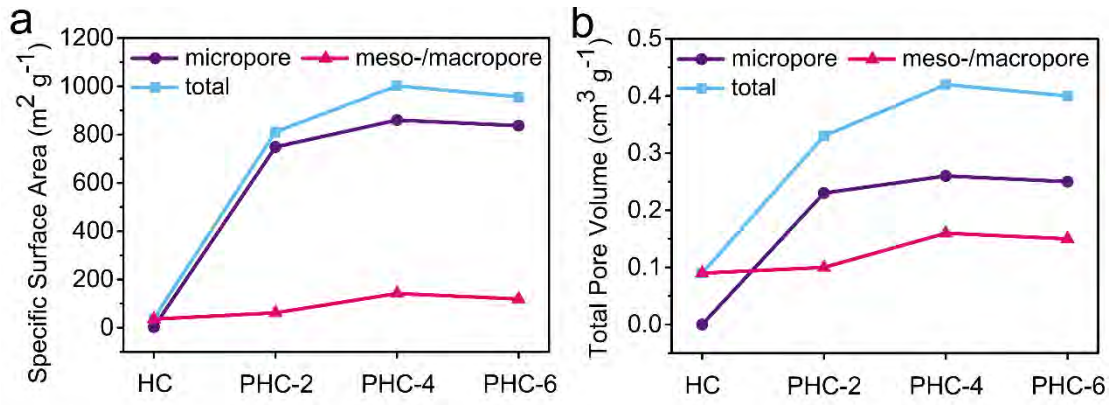

Fig. S5. (a) Effect of high-temperature carbonization followed by activation on specific surface area and particle density. (b) Effect of low-temperature carbonization followed by activation on specific surface area and particle density.

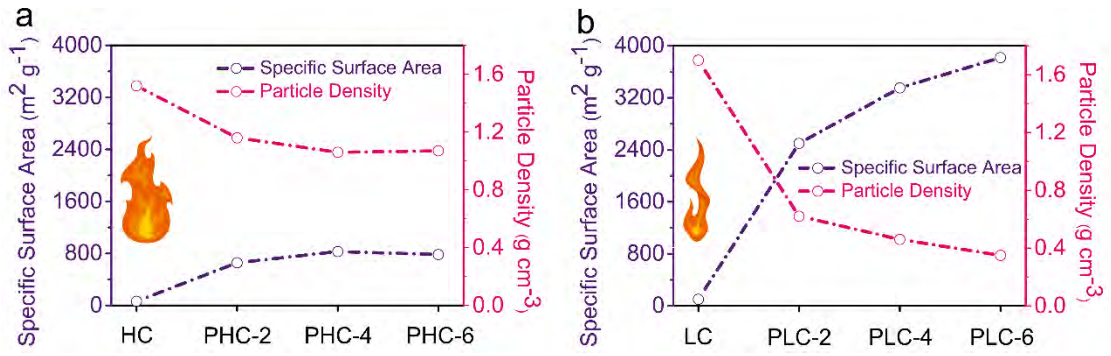

Fig. S6. Comparison of gravimetric capacitance at various scan rates in 6M KOH electrolyte in three-electrode configuration.

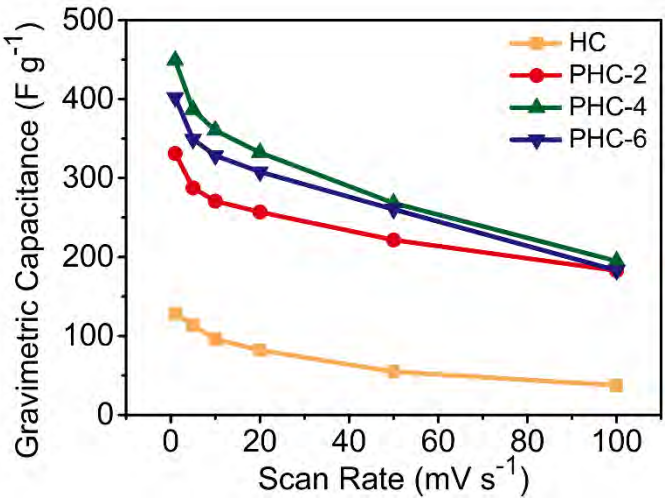

Fig. S7. (a) Detailed structure of PHC-4 symmetric supercapacitor. (b) Photographs of yellow LED powered by single PHC-4 based supercapacitor using 1M Li_2SO_4 electrolyte.

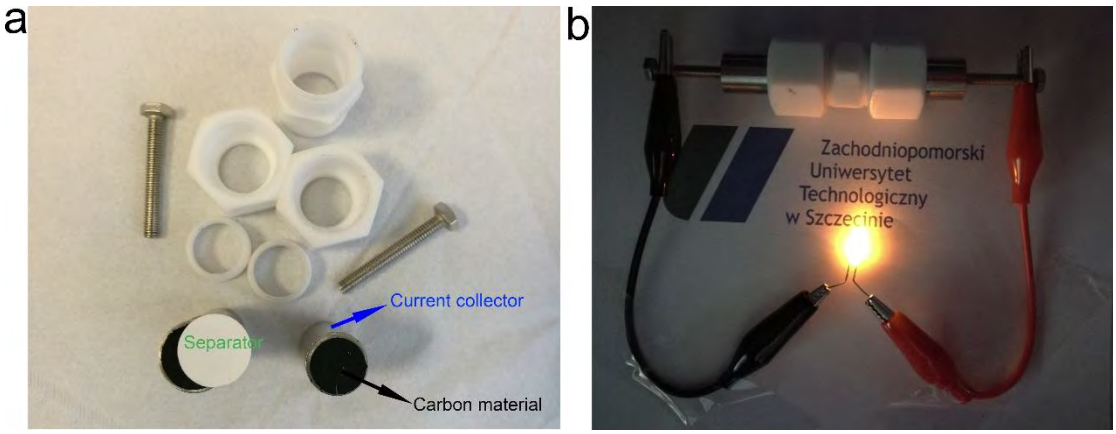

Table S1. Particle density of carbon samples calculated from Eq (2).

Sample	**HC**	**PHC-2**	**PHC-4**	**PHC-6**
True density ($g\ cm^{-3}$)	2.01	2.04	2.01	1.98
Pore volume ($cm^3\ g^{-1}$)	0.16	0.37	0.45	0.43
Particle density ($g\ cm^{-3}$)	1.52	1.16	1.06	1.07

Control group	**LC**	**PLC-2**	**PLC-4**	**PLC-6**
True density ($g\ cm^{-3}$)	1.97	2.00	2.04	2.02
Pore volume ($cm^3\ g^{-1}$)	0.08	1.11	1.70	2.34
Particle density ($g\ cm^{-3}$)	1.70	0.62	0.46	0.35

Table S2. Physical porosity parameters for Control groups.

Sample	S_{BET} ($m^2\ g^{-1}$)[a]	V_t ($cm^3\ g^{-1}$)[b]
LC	101	0.08
PLC-2	2499	1.11
PLC-4	3352	1.70
PLC-6	3818	2.34

[a] Brunaur-Emmett-Teller (BET) method is used to calculate the surface area.

[b] The total pore volume is determined at a relative pressure of 0.98.

Table S3. Comparison of the volumetric and gravimetric capacitances of biomass-derived carbon and high-density graphene materials.

Material	Specific surface area	Electrolyte	Volumetric Capacitance	Gravimetric Capacitance	R*	Ref
Auricularia	1103	6M KOH	360 $F\ cm^{-3}$	374 $F\ g^{-1}$	0.5 $A\ g^{-1}$	[1]
Kraft pulp	2045	6M KOH	310 $F\ cm^{-3}$	353 $F\ g^{-1}$	1 $A\ g^{-1}$	[2]
Perilla frutescens	655	6M KOH	287 $F\ cm^{-3}$	270 $F\ g^{-1}$	0.5 $A\ g^{-1}$	[3]
corn straw	1412	6M KOH	254 $F\ cm^{-3}$	299 $F\ g^{-1}$	5 $mV\ s^{-1}$	[4]
elm samara	1171	6M KOH	257 $F\ cm^{-3}$	470 $F\ g^{-1}$	1 $A\ g^{-1}$	[5]
seaweeds	270	1M H_2SO_4	180 $F\ cm^{-3}$	198 $F\ g^{-1}$	2 $mV\ s^{-1}$	[6]
kelp	1002	6M KOH	360 $F\ cm^{-3}$	440 $F\ g^{-1}$	0.5 $A\ g^{-1}$	[7]
Densely graphene/CNT	220	6M KOH	331 $F\ cm^{-3}$	294 $F\ g^{-1}$	5 $mV\ s^{-1}$	[8]
High-density graphene	370	6M KOH	376 $F\ cm^{-3}$	238 $F\ g^{-1}$	5 $mV\ s^{-1}$	[9]
jujube	829	6M KOH	476 $F\ cm^{-3}$ 410 $F\ cm^{-3}$ 382 $F\ cm^{-3}$	449 $F\ g^{-1}$ 387 $F\ g^{-1}$ 360 $F\ g^{-1}$	1 $mV\ s^{-1}$ 5 $mV\ s^{-1}$ 10 $mV\ s^{-1}$	This work

R*：Scan rate or Current density.

References

[1] C. Long, X. Chen, L. Jiang, L. Zhi, Z. Fan, Nano Energy, 12 (2015) 141-151.

[2] R.J. Mo, Y. Zhao, M.M. Zhao, M. Wu, C. Wang, J.P. Li, S. Kuga, Y. Huang, Chem Eng J, 346 (2018) 104-112.

[3] B. Liu, Y.J. Liu, H.B. Chen, M. Yang, H.M. Li, J Power Sources, 341 (2017) 309-317.

[4] Q.X. Xie, R.R. Bao, A.R. Zheng, Y.F. Zhang, S.H. Wu, C. Xie, P. Zhao, Acs Sustain Chem Eng, 4 (2016) 1422-1430.

[5] C. Chen, D.F. Yu, G.Y. Zhao, B.S. Du, W. Tang, L. Sun, Y. Sun, F. Besenbacher, M.

Yu, Nano Energy, 27 (2016) 377-389.

[6] E. Raymundo-Pinero, F. Leroux, F. Beguin, Advanced Materials, 18 (2006) 1877-+.

[7] J. Li, K. Liu, X. Gao, B. Yao, K.F. Huo, Y.L. Cheng, X.F. Cheng, D.C. Chen, B. Wang, W.M. Sun, D. Ding, M.L. Liu, L. Huang, Acs Appl Mater Inter, 7 (2015) 24622-24628.

[8] L.L. Jiang, L.Z. Sheng, C.L. Long, Z.J. Fan, Nano Energy, 11 (2015) 471-480.

[9] Y. Tao, X.Y. Xie, W. Lv, D.M. Tang, D.B. Kong, Z.H. Huang, H. Nishihara, T. Ishii, B.H. Li, D. Golberg, F.Y. Kang, T. Kyotani, Q.H. Yang, Sci Rep-Uk, 3 (2013).